1-31-2020

Generating Electromagnetic Dark and Antidark Partially Coherent Sources

Milo W. Hyde IV
Air Force Institute of Technology

Recommended Citation
Hyde, M. W. (2020). Generating electromagnetic dark and antidark partially coherent sources. Journal of Physics Communications, 4(1), 015025. https://doi.org/10.1088/2399-6528/ab6ed3

IOP Publishing J. Phys. Commun. 4 (2020) 015025 https://doi.org/10.1088/2399-6528/ab6ed3

Journal of Physics Communications

CrossMark

OPEN ACCESS

RECEIVED
10 January 2020

REVISED
17 January 2020

ACCEPTED FOR PUBLICATION
22 January 2020

PUBLISHED
30 January 2020

PAPER

Generating electromagnetic dark and antidark partially coherent sources

Milo W Hyde IV

Air Force Institute of Technology, 2950 Hobson Way, Dayton, OH 45433, United States of America

E-mail: milo.hyde@us.af.mil

Keywords: coherence, statistical optics, diffraction-free beams, vector sources

Supplementary material for this article is available online

Abstract

We present two methods to generate an electromagnetic dark and antidark partially coherent source. The first generalizes a recently published scalar approach by representing the stochastic electric field vector components as sums of randomly weighted, randomly tilted plane waves. The second method expands the field's vector components in series of randomly weighted dark and antidark coherent modes. The statistical moments of the random weights—plane waves in the former method, coherent modes in the latter—are found by comparing the resulting means and covariances to those of the desired electromagnetic dark and antidark source. We validate both methods by simulating the generation of an electromagnetic dark or antidark source and comparing the simulated results to the corresponding theoretical predictions. We find that both methods converge to the theoretical, ensemble-averaged (long-time-averaged) statistics within roughly 500 random field instances. The methods presented in this paper will find use in applications that utilize dark and antidark beams, e.g. atomic optics and optical trapping.

1. Introduction

Dark or antidark (DAD) beams are a type of dispersion-free or diffraction-free wave that has a dark or bright notch in on-axis intensity. These waves were first discovered as solitons in optical fibers [1, 2]. Ponomarenko *et al.* [3] showed that similar DAD waves can exist in linear media, granted the optical field is partially coherent.

Since that time, scalar DAD partially coherent sources (PCSs) have been experimentally realized using the source's coherent-mode representation [3, 4] and by passing a J_0-Bessel correlated PCS [5–7] through a wavefront-folding interferometer [8, 9]. In another recent paper, the authors showed that DAD beams could be realized from stochastic optical fields that are the weighted sums of randomly tilted plane waves [10].

Although a generalized, electromagnetic version of DAD beams was formulated shortly after Ponomarenko *et al.*'s original paper [11], to our knowledge, an electromagnetic DAD PCS has never been synthesized. [11] is very general and describes a whole class of diffraction-free, electromagnetic PCSs composed of uncorrelated Bessel beams, of which vector DAD beams are one example.

Here, we generate an example electromagnetic DAD beam discussed in [11] in two ways. The first extends the scalar approach presented in [10], where the vector components of the electric field are formed from the randomly weighted sums of randomly tilted plane waves. In the second approach, we expand the stochastic vector components of the electric field in sums of randomly weighted DAD coherent modes. In both methods, we find the statistics of the random weights by taking the auto- and cross-correlations of the field's vector components and comparing those correlations to the corresponding electromagnetic DAD source cross-spectral density (CSD) matrix elements.

In the next section, we present the statistical optics theory necessary to understand and implement both approaches. We then simulate the generation of an electromagnetic DAD PCS using both methods and compare the results to the corresponding theoretical expressions. Lastly, we conclude our work with a brief summary.

2. Theory

We begin with the electromagnetic DAD source CSD matrix $\underline{\mathbf{W}}$ given in equations (41) and (42) of [11]:

$$\begin{aligned} W_{\alpha\alpha}(\boldsymbol{\rho}_1, \boldsymbol{\rho}_2) &= J_0(\kappa|\boldsymbol{\rho}_1 - \boldsymbol{\rho}_2|) + \chi J_0(\kappa|\boldsymbol{\rho}_1 + \boldsymbol{\rho}_2|) \\ W_{xy}(\boldsymbol{\rho}_1, \boldsymbol{\rho}_2) &= aJ_0(\kappa|\boldsymbol{\rho}_1 - \boldsymbol{\rho}_2|), \end{aligned} \tag{1}$$

where $\alpha = x, y$, $\boldsymbol{\rho} = \hat{\mathbf{x}}x + \hat{\mathbf{y}}y$, $J_0(x)$ is a zeroth-order Bessel function of the first kind, κ is a real constant and related to the coherence width of the source, χ is a real constant subject to the constraint $|\chi| \leqslant 1$, and a is a complex constant such that $|a| \leqslant 1 - |\chi|$. The coherent-mode representation of the above electromagnetic DAD PCS is

$$\begin{aligned} W_{\alpha\alpha}(\boldsymbol{\rho}_1, \boldsymbol{\rho}_2) &= \sum_{n=-\infty}^{\infty} \lambda_n \Phi_n(\boldsymbol{\rho}_1)\Phi_n^*(\boldsymbol{\rho}_2) \\ W_{xy}(\boldsymbol{\rho}_1, \boldsymbol{\rho}_2) &= a\sum_{n=-\infty}^{\infty} \Phi_n(\boldsymbol{\rho}_1)\Phi_n^*(\boldsymbol{\rho}_2), \end{aligned} \tag{2}$$

where the eigenvalues λ_n and eigenfunctions Φ_n are

$$\begin{aligned} \lambda_n &= 1 + \chi(-1)^n \\ \Phi_n(\boldsymbol{\rho}) &= J_n(\kappa\rho)\exp(jn\phi). \end{aligned} \tag{3}$$

The propagation and polarization characteristics of these beams can be found in [3, 11].

2.1. Method 1: genuine CSD function criterion

In [10], using the genuine CSD function criterion [12, 13], the author showed that a scalar DAD source could be produced by summing many independent realizations of

$$U(\boldsymbol{\rho}) = \sqrt{\frac{1 + \sqrt{1 - \chi^2}}{2}}\left[\exp(j\kappa\mathbf{v}\cdot\boldsymbol{\rho}) + \frac{\chi}{1 + \sqrt{1 - \chi^2}}\exp(-j\kappa\mathbf{v}\cdot\boldsymbol{\rho})\right], \tag{4}$$

where $\mathbf{v} = \hat{\mathbf{x}}v\cos\theta + \hat{\mathbf{y}}v\sin\theta$ is a random vector. The radius v and angle θ are drawn from the following joint probability density (PDF) function:

$$p(\mathbf{v}) = p(\theta)p(v) = \frac{1}{2\pi}\delta(v - 1), \tag{5}$$

where $\delta(x)$ is the Dirac delta function.

To extend this method to produce the electromagnetic DAD source in equation (1), we let the electric field be

$$\mathbf{E}(\boldsymbol{\rho}) = \hat{\mathbf{x}}E_x(\boldsymbol{\rho}) + \hat{\mathbf{y}}E_y(\boldsymbol{\rho}), \tag{6}$$

where the stochastic vector components are

$$E_\alpha(\boldsymbol{\rho}) = b_\alpha\exp(j\kappa\mathbf{v}\cdot\boldsymbol{\rho}) + c_\alpha\exp(-j\kappa\mathbf{v}\cdot\boldsymbol{\rho}). \tag{7}$$

In equation (7), the b_α and c_α are complex random numbers. This stands in contrast to the scalar case, where the plane wave coefficients are deterministic [see equation (4)].

Taking the auto-correlation of equation (7) and assuming that b_α and c_α are statistically independent of $\mathbf{v}$ yields

$$\begin{aligned} W_{\alpha\alpha}(\boldsymbol{\rho}_1, \boldsymbol{\rho}_2) = &\langle b_\alpha b_\alpha^*\rangle\langle\exp(j\kappa\mathbf{v}\cdot\boldsymbol{\rho}_d)\rangle + \langle c_\alpha c_\alpha^*\rangle\langle\exp(-j\kappa\mathbf{v}\cdot\boldsymbol{\rho}_d)\rangle \\ &+ \langle b_\alpha c_\alpha^*\rangle\langle\exp(j\kappa\mathbf{v}\cdot\boldsymbol{\rho}_a)\rangle + \langle b_\alpha^* c_\alpha\rangle\langle\exp(-j\kappa\mathbf{v}\cdot\boldsymbol{\rho}_a)\rangle, \end{aligned} \tag{8}$$

where $\boldsymbol{\rho}_{a,d} = \boldsymbol{\rho}_1 \pm \boldsymbol{\rho}_2$. The moments containing the complex exponentials are equivalent to the joint characteristic functions of $\mathbf{v}$. Using the joint PDF in equation (5), these moments are easy to compute, and equation (8) simplifies to

$$W_{\alpha\alpha}(\boldsymbol{\rho}_1, \boldsymbol{\rho}_2) = (\langle b_\alpha b_\alpha^*\rangle + \langle c_\alpha c_\alpha^*\rangle)J_0(\kappa\rho_d) + 2\,\mathrm{Re}(\langle b_\alpha c_\alpha^*\rangle)J_0(\kappa\rho_a). \tag{9}$$

Comparing equations (1) and (9) and expanding b_α and c_α into real and imaginary parts reveals the following equalities:

$$\begin{aligned} \langle(b_\alpha^{\mathrm{r}})^2\rangle + \langle(b_\alpha^{\mathrm{i}})^2\rangle + \langle(c_\alpha^{\mathrm{r}})^2\rangle + \langle(c_\alpha^{\mathrm{i}})^2\rangle &= 1 \\ \langle b_\alpha^{\mathrm{r}} c_\alpha^{\mathrm{r}}\rangle + \langle b_\alpha^{\mathrm{i}} c_\alpha^{\mathrm{i}}\rangle &= \chi/2. \end{aligned} \tag{10}$$

For simplicity, we let the variances and covariances on the left-hand sides of equation (10) be equal producing

$$\begin{aligned} \langle (b_\alpha^{\mathrm{r}})^2 \rangle &= \langle (b_\alpha^{\mathrm{i}})^2 \rangle = \langle (c_\alpha^{\mathrm{r}})^2 \rangle = \langle (c_\alpha^{\mathrm{i}})^2 \rangle = 1/4 \\ \langle b_\alpha^{\mathrm{r}} c_\alpha^{\mathrm{r}} \rangle &= \langle b_\alpha^{\mathrm{i}} c_\alpha^{\mathrm{i}} \rangle = \chi/4. \end{aligned} \tag{11}$$

Referring back to equation (7), we now take the cross-correlation of E_x and E_y yielding

$$\begin{aligned} W_{xy}(\boldsymbol{\rho}_1, \boldsymbol{\rho}_2) &= \langle b_x b_y^* \rangle \langle \exp(\mathrm{j}\kappa \boldsymbol{v} \cdot \boldsymbol{\rho}_d) \rangle + \langle c_x c_y^* \rangle \langle \exp(-\mathrm{j}\kappa \boldsymbol{v} \cdot \boldsymbol{\rho}_d) \rangle \\ &\quad + \langle b_x c_y^* \rangle \langle \exp(\mathrm{j}\kappa \boldsymbol{v} \cdot \boldsymbol{\rho}_a) \rangle + \langle b_y^* c_x \rangle \langle \exp(-\mathrm{j}\kappa \boldsymbol{v} \cdot \boldsymbol{\rho}_a) \rangle \\ &= (\langle b_x b_y^* \rangle + \langle c_x c_y^* \rangle) J_0(\kappa \rho_d) + (\langle b_x c_y^* \rangle + \langle b_y^* c_x \rangle) J_0(\kappa \rho_a). \end{aligned} \tag{12}$$

Comparing the above W_{xy} to the desired one in equation (1) reveals

$$\begin{aligned} \langle b_x^{\mathrm{r}} b_y^{\mathrm{r}} \rangle + \langle b_x^{\mathrm{i}} b_y^{\mathrm{i}} \rangle + \langle c_x^{\mathrm{r}} c_y^{\mathrm{r}} \rangle + \langle c_x^{\mathrm{i}} c_y^{\mathrm{i}} \rangle &= a^{\mathrm{r}} \\ \langle b_x^{\mathrm{i}} b_y^{\mathrm{r}} \rangle - \langle b_x^{\mathrm{r}} b_y^{\mathrm{i}} \rangle + \langle c_x^{\mathrm{i}} c_y^{\mathrm{r}} \rangle - \langle c_x^{\mathrm{r}} c_y^{\mathrm{i}} \rangle &= a^{\mathrm{i}} \\ \langle b_x^{\mathrm{r}} c_y^{\mathrm{r}} \rangle + \langle b_x^{\mathrm{i}} c_y^{\mathrm{i}} \rangle + \langle c_x^{\mathrm{r}} b_y^{\mathrm{r}} \rangle + \langle c_x^{\mathrm{i}} b_y^{\mathrm{i}} \rangle &= 0 \\ \langle b_x^{\mathrm{i}} c_y^{\mathrm{r}} \rangle - \langle b_x^{\mathrm{r}} c_y^{\mathrm{i}} \rangle + \langle c_x^{\mathrm{i}} b_y^{\mathrm{r}} \rangle - \langle c_x^{\mathrm{r}} b_y^{\mathrm{i}} \rangle &= 0. \end{aligned} \tag{13}$$

For simplicity, we let

$$\begin{aligned} \langle b_x^{\mathrm{r}} b_y^{\mathrm{r}} \rangle = \langle b_x^{\mathrm{i}} b_y^{\mathrm{i}} \rangle = \langle c_x^{\mathrm{r}} c_y^{\mathrm{r}} \rangle = \langle c_x^{\mathrm{i}} c_y^{\mathrm{i}} \rangle &= a^{\mathrm{r}}/4 \\ \langle b_x^{\mathrm{i}} b_y^{\mathrm{r}} \rangle = \langle c_x^{\mathrm{i}} c_y^{\mathrm{r}} \rangle = -\langle b_x^{\mathrm{r}} b_y^{\mathrm{i}} \rangle = -\langle c_x^{\mathrm{r}} c_y^{\mathrm{i}} \rangle &= a^{\mathrm{i}}/4 \\ \langle b_x^{\mathrm{r}} c_y^{\mathrm{r}} \rangle = \langle b_x^{\mathrm{i}} c_y^{\mathrm{i}} \rangle = \langle c_x^{\mathrm{r}} b_y^{\mathrm{r}} \rangle = \langle c_x^{\mathrm{i}} b_y^{\mathrm{i}} \rangle &= 0 \\ \langle b_x^{\mathrm{i}} c_y^{\mathrm{r}} \rangle = \langle b_x^{\mathrm{r}} c_y^{\mathrm{i}} \rangle = \langle c_x^{\mathrm{i}} b_y^{\mathrm{r}} \rangle = \langle c_x^{\mathrm{r}} b_y^{\mathrm{i}} \rangle &= 0 \end{aligned} \tag{14}$$

to complete the derivation.

Note that we chose the second moment values in equations (11) and (14) solely for convenience. Any values that satisfy the linear constraint equations in equations (10) and (13), as well as the conditions on χ and a specified below equation (1), are valid.

In summary, an electromagnetic DAD PCS with a CSD matrix given in equation (1) can be produced by incoherently summing stochastic vector fields, whose components take the form of equation (7). The radius v and angle θ of the random vector $\boldsymbol{v}$ are drawn from the joint PDF given in equation (5). Lastly, the random complex coefficients b_α and c_α are zero mean and have a covariance matrix $\underline{\mathbf{K}}$ equal to

$$\underline{\mathbf{K}} = \left\langle \begin{bmatrix} b_x \\ c_x \\ b_y \\ c_y \end{bmatrix} \begin{bmatrix} b_x^* & c_x^* & b_y^* & c_y^* \end{bmatrix} \right\rangle = \frac{1}{4} \begin{bmatrix} 1 & 0 & \chi & 0 & a^{\mathrm{r}} & -a^{\mathrm{i}} & 0 & 0 \\ 0 & 1 & 0 & \chi & a^{\mathrm{i}} & a^{\mathrm{r}} & 0 & 0 \\ \chi & 0 & 1 & 0 & 0 & 0 & a^{\mathrm{r}} & -a^{\mathrm{i}} \\ 0 & \chi & 0 & 1 & 0 & 0 & a^{\mathrm{i}} & a^{\mathrm{r}} \\ a^{\mathrm{r}} & a^{\mathrm{i}} & 0 & 0 & 1 & 0 & \chi & 0 \\ -a^{\mathrm{i}} & a^{\mathrm{r}} & 0 & 0 & 0 & 1 & 0 & \chi \\ 0 & 0 & a^{\mathrm{r}} & a^{\mathrm{i}} & \chi & 0 & 1 & 0 \\ 0 & 0 & -a^{\mathrm{i}} & a^{\mathrm{r}} & 0 & \chi & 0 & 1 \end{bmatrix}. \tag{15}$$

The statistical distributions of b_α and c_α are irrelevant as long as the first and second moments are equal to those specified above. Because it is easy to generate correlated normal random numbers, we recommend letting b_α and c_α be jointly Gaussian distributed.

2.2. Method 2: coherent modes

Here, we expand E_x and E_y in series of DAD coherent modes, where the coherent mode weights are complex random numbers.

We note that a similar expansion was first employed by Kim and Wolf [14], although for a different purpose. By treating the Hermitian CSD matrix $\underline{\mathbf{W}}$ diagonal elements (W_{xx} and W_{yy}) as scalar PCSs and expanding each in two distinct sets of orthogonal coherent modes, Kim and Wolf were able to derive a bi-modal (double series) expansion for the non-Hermitian off-diagonal elements. This procedure, requiring the solutions of two uncoupled integral equations to find the modes of W_{xx} and W_{yy}, is considerably simpler than the traditional approach, which requires solving a set of coupled integral equations. Of course, the price paid for this simplicity is the double series representation for W_{xy}.

In our case however, because W_{xx} and W_{yy} have the same coherent modes [see equation (2)], this approach turns out to be quite convenient. We begin by expanding E_x and E_y as

$$\begin{aligned} E_x(\boldsymbol{\rho}) &= \textstyle\sum_{n=-\infty}^{\infty} b_n \Phi_n(\boldsymbol{\rho}) \\ E_y(\boldsymbol{\rho}) &= \textstyle\sum_{n=-\infty}^{\infty} c_n \Phi_n(\boldsymbol{\rho}), \end{aligned} \tag{16}$$

where Φ_n is defined in equation (3) and b_n and c_n are random complex numbers drawn from some arbitrary distribution.

It is important to emphasize that this approach is fundamentally different to using coherent modes to generate scalar PCSs. In the latter, the deterministic field consists of a single weighted mode. The scalar PCS is formed by summing the weighted modes incoherently typically at the detector [4, 15, 16]. Here, a stochastic field realization is formed from the randomly weighted, coherent addition of many modes. The electromagnetic PCS is formed by incoherently summing many statistically independent vector field realizations.

Taking the auto-correlation of equation (16) yields

$$W_{xx}(\boldsymbol{\rho}_1, \boldsymbol{\rho}_2) = \sum_{n=-\infty}^{\infty} \sum_{m=-\infty}^{\infty} \langle b_n b_m^* \rangle \Phi_n(\boldsymbol{\rho}_1) \Phi_m^*(\boldsymbol{\rho}_2), \tag{17}$$

with a similar expression for W_{yy}. Comparing this expression (and the W_{yy} expression) to the coherent-mode representation in equation (2) reveals that

$$\langle b_n b_m^* \rangle = \langle c_n c_m^* \rangle = \lambda_n \delta_{nm}, \tag{18}$$

where δ_{nm} is the Kronecker delta function.

We now turn our attention to the off-diagonal elements. Taking the cross-correlation of the vector components in equation (16) produces

$$W_{xy}(\boldsymbol{\rho}_1, \boldsymbol{\rho}_2) = \sum_{n=-\infty}^{\infty} \sum_{m=-\infty}^{\infty} \langle b_n c_m^* \rangle \Phi_n(\boldsymbol{\rho}_1) \Phi_m^*(\boldsymbol{\rho}_2). \tag{19}$$

Comparing this expression to W_{xy} in equation (2) reveals the following:

$$\langle b_n c_m^* \rangle = a \delta_{nm}. \tag{20}$$

We note that because of the Kronecker delta functions in equations (18) and (20), there is no coupling between different index modes in equation (16). Taking this into account and expanding b_n and c_n in real and imaginary parts produces

$$\begin{aligned} \langle (b_n^{\mathrm{r}})^2 \rangle + \langle (b_n^{\mathrm{i}})^2 \rangle &= \lambda_n \\ \langle (c_n^{\mathrm{r}})^2 \rangle + \langle (c_n^{\mathrm{i}})^2 \rangle &= \lambda_n \\ \langle b_n^{\mathrm{r}} c_n^{\mathrm{r}} \rangle + \langle b_n^{\mathrm{i}} c_n^{\mathrm{i}} \rangle &= a^{\mathrm{r}} \\ \langle b_n^{\mathrm{i}} c_n^{\mathrm{r}} \rangle - \langle b_n^{\mathrm{r}} c_n^{\mathrm{i}} \rangle &= a^{\mathrm{i}}. \end{aligned} \tag{21}$$

Again, for simplicity, we let

$$\begin{aligned} \langle (b_n^{\mathrm{r}})^2 \rangle = \langle (b_n^{\mathrm{i}})^2 \rangle &= \lambda_n/2 \\ \langle (c_n^{\mathrm{r}})^2 \rangle = \langle (c_n^{\mathrm{i}})^2 \rangle &= \lambda_n/2 \\ \langle b_n^{\mathrm{r}} c_n^{\mathrm{r}} \rangle = \langle b_n^{\mathrm{i}} c_n^{\mathrm{i}} \rangle &= a^{\mathrm{r}}/2 \\ \langle b_n^{\mathrm{i}} c_n^{\mathrm{r}} \rangle = -\langle b_n^{\mathrm{r}} c_n^{\mathrm{i}} \rangle &= a^{\mathrm{i}}/2. \end{aligned} \tag{22}$$

Like in method 1, the values specified for the second moments in equation (22) are chosen for convenience. Any values that satisfy the linear constraint equations in equation (21) and the χ and a conditions stated above are valid.

Summarizing this method, an electromagnetic DAD PCS with a CSD matrix given in equation (1) can be generated by incoherently summing many realizations of the E_x and E_y given in equation (16). The means and covariances of b_n and c_n are zero and

$$\underline{\mathbf{K}} = \left\langle \begin{bmatrix} b_n \\ c_n \end{bmatrix} \begin{bmatrix} b_n^* & c_n^* \end{bmatrix} \right\rangle = \frac{1}{2} \begin{bmatrix} \lambda_n & 0 & a^{\mathrm{r}} & -a^{\mathrm{i}} \\ 0 & \lambda_n & a^{\mathrm{i}} & a^{\mathrm{r}} \\ a^{\mathrm{r}} & a^{\mathrm{i}} & \lambda_n & 0 \\ -a^{\mathrm{i}} & a^{\mathrm{r}} & 0 & \lambda_n \end{bmatrix}. \tag{23}$$

Like method 1, the distributions of b_n and c_n are irrelevant as long as the means are zero and the covariance matrix equals equation (23). Again, Gaussian random numbers are a very convenient choice.

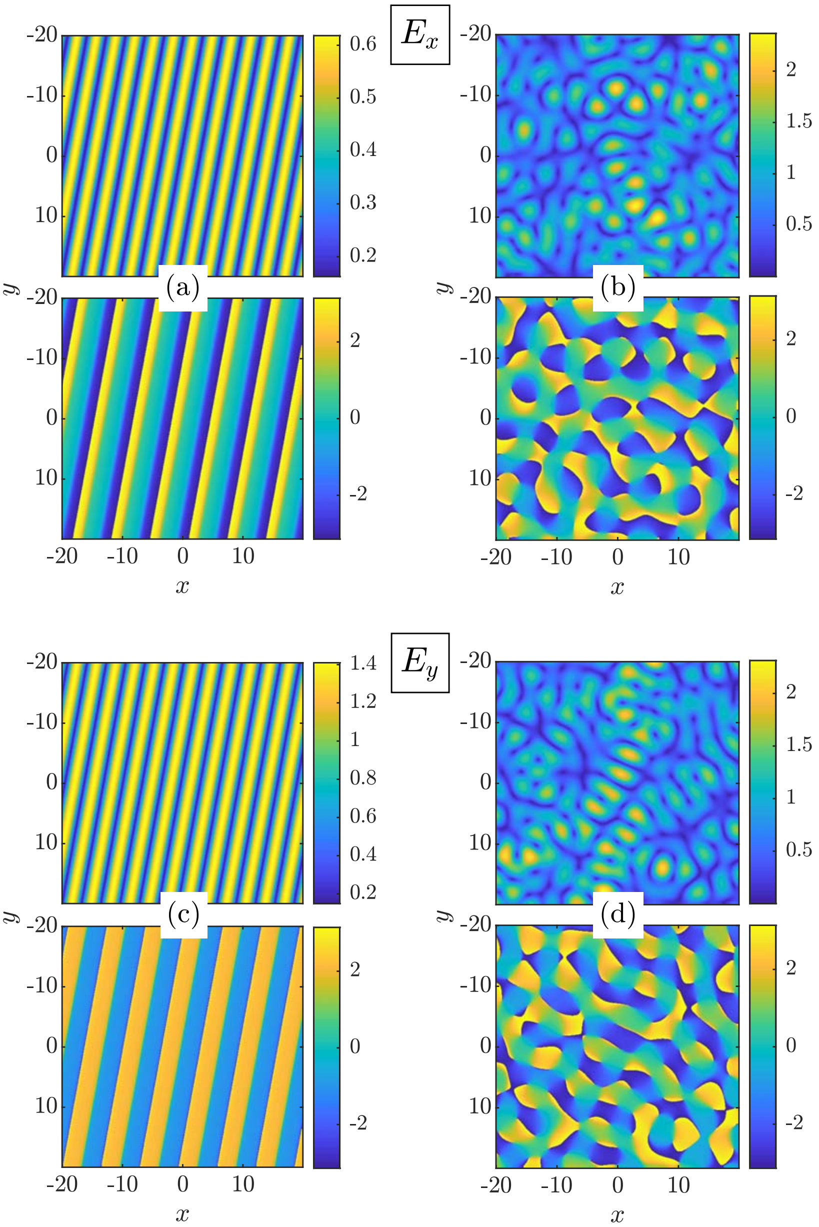

Figure 1. Field realizations for methods 1 and 2 [equations (7) and (16), respectively]—(a) method 1 $|E_x|$ (top) and $\arg(E_x)$ (bottom), (b) method 2 $|E_x|$ (top) and $\arg(E_x)$ (bottom), (c) method 1 $|E_y|$ (top) and $\arg(E_y)$ (bottom), and (d) method 2 $|E_y|$ (top) and $\arg(E_y)$ (bottom).

3. Simulation

In this section, we simulate the generation of an electromagnetic DAD PCS with $\chi = -0.8$, $a = 0.2\exp(\mathrm{j}\pi/4)$, and $\kappa = 1$ unit^{-1} using both methods derived in section 2. In the field expressions for methods 1 and 2 [equations (7) and (16), respectively], κ (recall that κ is related to the coherence width of the source) scales the physical vector $\boldsymbol{\rho}$. Therefore, the features of electromagnetic DAD beams shown in the results below are simply magnified (or demagnified) by varying κ.

As we show in the accompanying MATLAB® simulation code, we used square computational grids that were $L = 40$ units in width and 512 points on a side. For both methods, we generated 50,000 stochastic field realizations to compute the spectral densities $S(\boldsymbol{\rho}) = W_{xx}(\boldsymbol{\rho}, \boldsymbol{\rho}) + W_{yy}(\boldsymbol{\rho}, \boldsymbol{\rho})$ and two-dimensional planar cuts of the CSD matrix $\underline{\mathbf{W}}(x_1, 0, x_2, 0)$. Prior scalar DAD source work showed that 50–60 modes were sufficient to accurately represent the PCS [3, 4]. To create high-fidelity stochastic fields, we used 121 modes ($n = -60, -59, \cdots, 60$) in the expansions in equation (16).

Figure 1 shows stochastic electromagnetic DAD field realizations (magnitudes and phases of E_x and E_y) for both methods 1 and 2. Recall that for method 1, a DAD stochastic vector component realization is the sum of randomly tilted 'forward' [positive complex exponential in equation (7)] and 'reverse' [negative complex

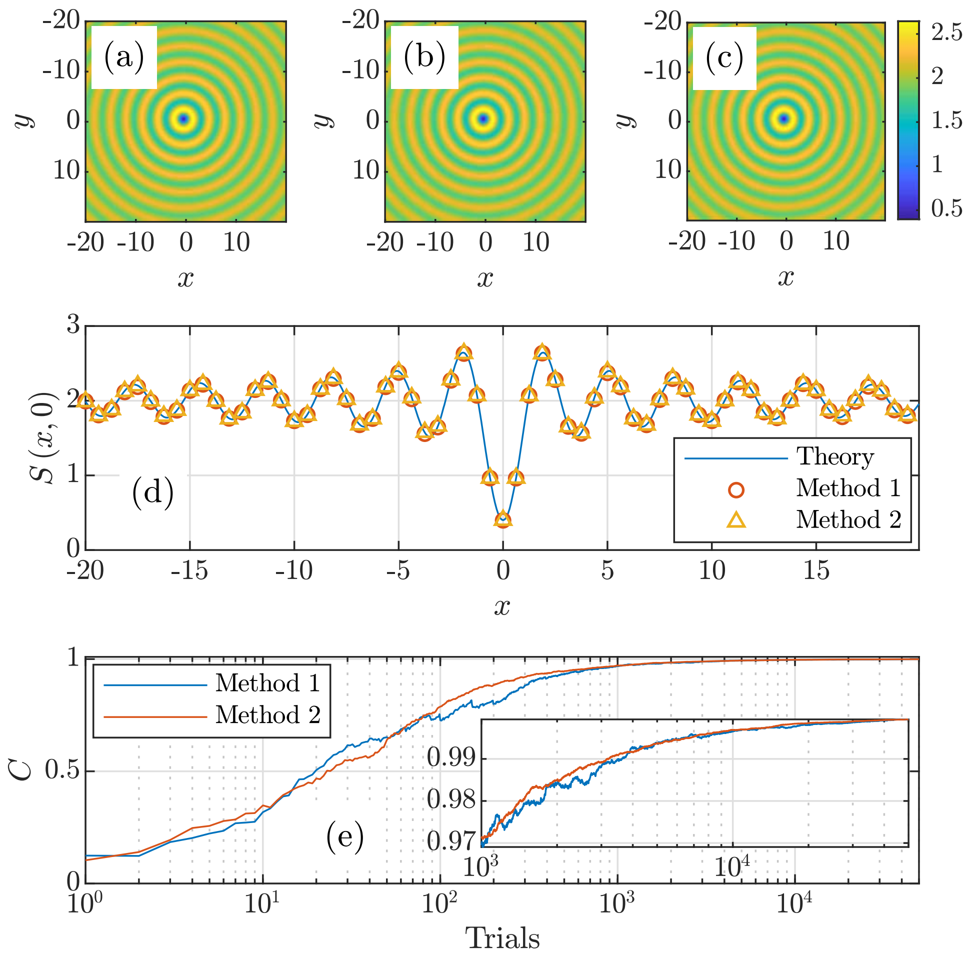

Figure 2. Spectral density S results—(a) theory, (b) method 1, (c) method 2, (d) $y = 0$ slices through the theoretical, method 1, and method 2 S, and (e) two-dimensional correlation coefficients C for methods 1 and 2 S computed against S theory versus trial number. The inset in (e) shows C from trials 1,000–50,000.

exponential in equation (7)] plane waves. Like the tilt (or direction), the amplitudes of the forward and reverse planes waves are also random.

Note that this is precisely the field that is shown in figures 1(a) and (c). The grating-like, or standing-wave behaviors in figures 1(a) and (c) are due to the coherent addition (interference) of the forward and reverse plane waves in E_x and E_y. The interference patterns in E_x and E_y are oriented in the same direction. This will always be the case, as this is required to produce the CSD matrix elements in equation (1); however, the 'grating' direction will change from field realization to field realization. Likewise, the amplitudes of E_x and E_y, being random, will change from field realization to field realization.

For method 2, a DAD stochastic vector component realization is the sum of randomly weighted DAD coherent modes, or equivalently, Bessel beams. It is the coherent sums of these randomly weighted Bessel beams that is responsible for the patterns in figures 1(b) and (d). The branch points (phase vortices) evident in the lower images of figures 1(b) and (d) occur at points of perfect destructive interference (amplitude or intensity nulls). These branch point locations and more generally, the interference patterns themselves, will change with the random weights [b_n and c_n in equation (16)] from field realization to field realization.

Figures 2 and 3 shows the spectral density S and CSD matrix $\underline{\mathbf{W}}(x_1, 0, x_2, 0)$ results, respectively. In figures 2(a), (b), and (c) show the theoretical, method 1, and method 2 S. All are plotted using the same color scale defined by the color bar to the right of figure 2(c). Figure 2(d) shows the $y = 0$ slices $S(x, 0)$ through (a), (b), and (c) on the same plot for comparison, and (e) shows the two-dimensional correlation coefficients C for the methods 1 and 2 S computed against S theory versus trial number. The inset in figure 2(e) shows C from trials 1,000–50,000. C was computed using

$$C = \frac{\sum_{k=1}^{N^2}(S^{\text{sim}}[k] - \bar{S}^{\text{sim}})(S^{\text{thy}}[k] - \bar{S}^{\text{thy}})}{\sqrt{\sum_{k=1}^{N^2}(S^{\text{sim}}[k] - \bar{S}^{\text{sim}})^2}\sqrt{\sum_{k=1}^{N^2}(S^{\text{thy}}[k] - \bar{S}^{\text{thy}})^2}}, \tag{24}$$

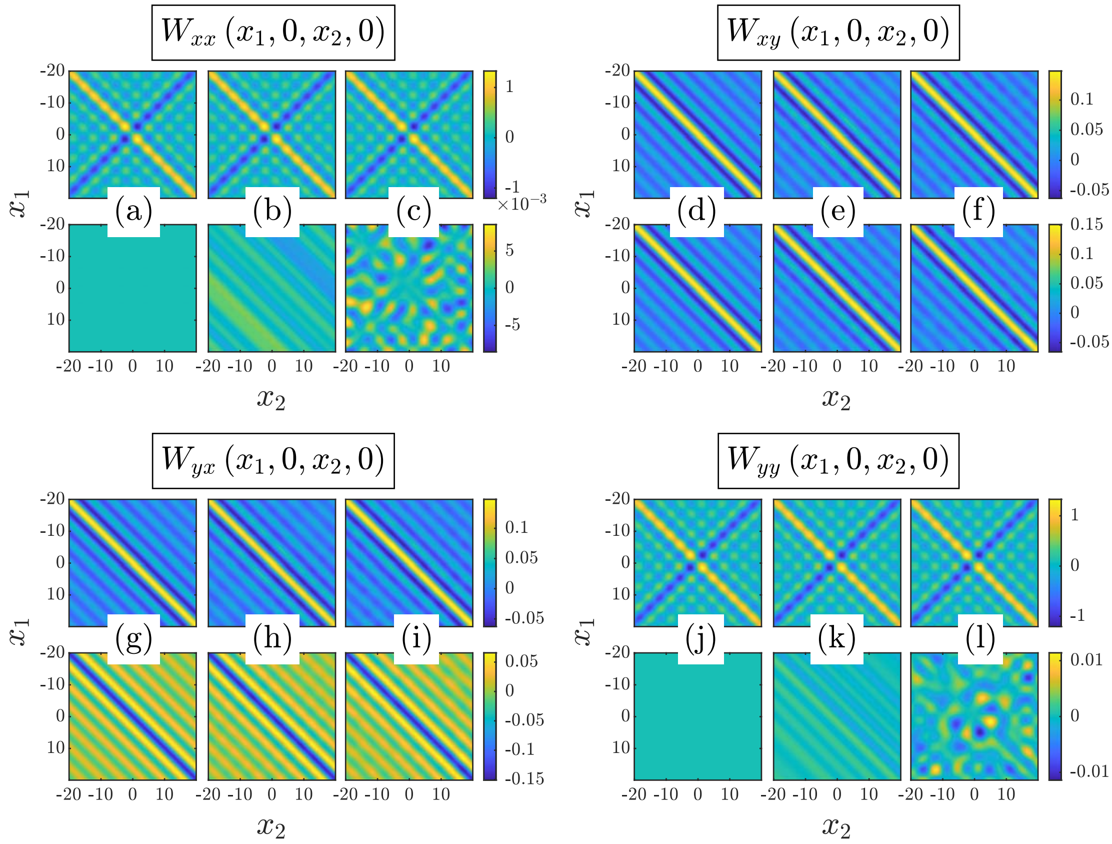

Figure 3. $\underline{\mathbf{W}}(x_1, 0, x_2, 0)$ results—real (top) and imaginary (bottom) parts of W_{xx} (a) theory, (b) method 1, (c) method 2; real (top) and imaginary (bottom) parts of W_{xy} (d) theory, (e) method 1, (f) method 2; real (top) and imaginary (bottom) parts of W_{yx} (g) theory, (h) method 1, (i) method 2; and real (top) and imaginary (bottom) parts of W_{yy} (j) theory, (k) method 1, (l) method 2.

where $N^2 = 512^2$ was the total number of pixels in an image, $\bar{S}$ was the average value of the spectral density, and k was a discrete pixel index.

Figure 3 is organized like the 2×2 CSD matrix $\underline{\mathbf{W}}$. Each $\underline{\mathbf{W}}$ 'element' consists of 6 images arranged in 2 rows and 3 columns and is labeled for the reader's convenience. The theoretical, method 1, and method 2 $\underline{\mathbf{W}}(x_1, 0, x_2, 0)$ are shown in columns 1–3 of each element, respectively. Rows 1 and 2 show the real and imaginary parts of $\underline{\mathbf{W}}$. The images in rows 1 and 2 are plotted on the same false color scales defined by the respective color bars at rows' end.

The agreement between theory and simulation for both methods is excellent. The results in figures 2 and 3 show that both methods produce an electromagnetic DAD source with the proper shape and correlation (coherence) properties, respectively. In addition, figure 2(e) shows that both approaches converge to the theoretical, or desired source after integrating 500 stochastic field realizations. We note that electromagnetic DAD PCSs radiate diffraction-free beams and therefore, the shapes of the spectral density and CSD matrix elements pictured in figures 2 and 3 do not change upon propagation.

4. Conclusion

In this paper, we presented two methods to produce an electromagnetic dark and antidark (DAD) partially coherent source (PCS). The first, extending a recently published scalar DAD PCS method [10], represented the field's vector components, E_x and E_y, as sums of randomly weighted, randomly tilted plane waves. The second expanded E_x and E_y in series of randomly weighted DAD coherent modes. By comparing the stochastic fields' auto- and cross-correlations to the theoretical DAD source CSD matrix, we were able to generate realizations of the random weights using a multivariate Gaussian random number generator.

We simulated the generation of an electromagnetic DAD source using both methods and validated our analysis by comparing the simulated spectral densities and CSD matrices to their theoretical counterparts. The agreement between simulation and theory was excellent. In addition, we found that both approaches converged to the theoretical moments within 500 stochastic field realizations. This finding will be useful to those who implement these methods for a specific application.

Lastly, we note that both methods presented in this paper can be implemented on vector beam generators that utilize one or two spatial light modulators [17–20]. Our work will find use in applications germane to DAD beams, e.g. atomic optics and optical trapping.

Acknowledgments

The views expressed in this paper are those of the authors and do not reflect the official policy or position of the U.S. Air Force, the Department of Defense, or the U.S. Government.

ORCID iDs

Milo W Hyde IV https://orcid.org/0000-0003-2814-202X

References

[1] Kodama Y and Hasegawa A 1992 Theoretical foundation of optical-soliton concept in fibers *Prog. Opt.* vol 30 ed E Wolf (Amsterdam: Elsevier) ch 4 pp 205–59
[2] Kivshar Y S and Luther-Davies B 1998 *Phys. Rep.* **298** 81–197
[3] Ponomarenko S A, Huang W and Cada M 2007 *Opt. Lett.* **32** 2508–10
[4] Zhu X, Wang F, Zhao C, Cai Y and Ponomarenko S A 2019 *Opt. Lett.* **44** 2260–3
[5] Gori F, Guattari G and Padovani C 1987 *Opt. Commun.* **64** 311–6
[6] Korotkova O 2014 *Random Light Beams: Theory and Applications* (Boca Raton, FL: CRC)
[7] Mandel L and Wolf E 1995 *Optical Coherence and Quantum Optics* (New York, NY: Cambridge University)
[8] Turunen J, Vasara A and Friberg A T 1991 *J. Opt. Soc. Am.* A **8** 282–9
[9] Partanen H, Sharmin N, Tervo J and Turunen J 2015 *Opt. Express* **23** 28718–27
[10] Hyde M W and Avramov-Zamurovic S 2019 *J. Opt. Soc. Am.* A **36** 1058–63
[11] Borghi R, Gori F and Ponomarenko S A 2009 *J. Opt. Soc. Am.* A **26** 2275–81
[12] Gori F and Santarsiero M 2007 *Opt. Lett.* **32** 3531–3
[13] Martínez-Herrero R, Mejías P M and Gori F 2009 *Opt. Lett.* **34** 1399–401
[14] Kim K and Wolf E 2006 *Opt. Commun.* **261** 19–22
[15] Bhattacharjee A, Sahu R and Jha A K 2019 *J. Opt.* **21** 105601
[16] Chen X, Li J, Rafsanjani S M H and Korotkova O 2018 *Opt. Lett.* **43** 3590–3
[17] Hyde M W, Bose-Pillai S, Voelz D G and Xiao X 2016 *Phys. Rev. Applied* **6** 064030
[18] Chen Z, Zeng T, Qian B and Ding J 2015 *Opt. Express* **23** 17701–10
[19] Yu Z, Chen H, Chen Z, Hao J and Ding J 2015 *Opt. Commun.* **345** 135–40
[20] Rosales-Guzmán C, Bhebhe N and Forbes A 2017 *Opt. Express* **25** 25697–706